



Molecular dynamics study of mechanical behavior of gold-silicon core-shell nanowires under cyclic loading

Julien Godet, Laurent Pizzagalli, Maxime Guillotte

► To cite this version:

Julien Godet, Laurent Pizzagalli, Maxime Guillotte. Molecular dynamics study of mechanical behavior of gold-silicon core-shell nanowires under cyclic loading. *Acta Materialia*, 2019, 5, pp.100204. 10.1016/j.mtla.2018.100204 . hal-02136332

HAL Id: hal-02136332

<https://hal.science/hal-02136332>

Submitted on 22 May 2019

HAL is a multi-disciplinary open access archive for the deposit and dissemination of scientific research documents, whether they are published or not. The documents may come from teaching and research institutions in France or abroad, or from public or private research centers.

L'archive ouverte pluridisciplinaire **HAL**, est destinée au dépôt et à la diffusion de documents scientifiques de niveau recherche, publiés ou non, émanant des établissements d'enseignement et de recherche français ou étrangers, des laboratoires publics ou privés.

Molecular dynamics study of mechanical behavior of gold-silicon core-shell nanowires under cyclic loading

Maxime Guillotte, Julien Godet, Laurent Pizzagalli

Departement of Physics and Mechanics of Materials, Institut Pprime, CNRS, Université de Poitiers, TSA 41123, 86073 Poitiers Cedex 9, France

Abstract

Composite systems at nanoscale are promising to design new materials combining different interesting properties, like high strength and good plasticity. In the present work, we compare mechanical properties of gold-silicon core-shell and pure gold nanowires subjected to several tensile loadings and compressive unloadings at 300 K and 1 K, in order to evaluate the ability of a hard amorphous silicon shell to stabilize a crystalline gold core during cyclic loading. The hard shell appears involved in the quasi-reversible macroscopic plasticity of core-shell NW, by promoting twins, stacking fault and isolated full dislocations, due to a confinement effect of the core. In addition, our simulations revealed that the reversible behavior is progressively lost over cycles. The analysis of the amorphous shell shows that large strains combined with high strain rate prevent self-healing of the shell, leading to shell failure and to reversibility loss.

Keywords: reversible plasticity, shape restoration , Simulation, Amorphous silicon, Cyclic strain , composite materials, interface

1. Introduction

New technologies often rely on multifunctional materials combining at least two interesting properties for applications, e.g. low density and high strength, high conductivity and high wear-resistance, or high strength and good ductility [1]. However, these properties are usually antagonistic or cannot co-exist. Using composite materials is one promising solution to design such multifunctional materials. It is particularly true at the nanoscale, where the ratios of surface on volume and/or interface on volume become predominant and allow to tune physical properties. For almost two decades, the fast development of experimental techniques for designing and testing nanostructures allows to reveal remarkable modifications of physical properties at nanoscale compared to their bulk counterparts, notably regarding mechanical aspects [2]. The high

strength sustained by such nanostructures has been thought to be used in composite materials to make them stronger [3, 4, 5].

Examples of interesting core-shell systems are Ti-TiN nanostructures, which exhibit high strength, high thermal stability, and good plasticity properties [6], core-shell nanowires (NWs) with increased Young modulus [7], or core-shell nanoparticles [8, 9]. Other more complex composite nanostructures, such as nanoporous gold covered by a thin layer of hard oxide, have been shown to limit coarsening and to enhance the materials strength [10]. The latter effect has been recently investigated in core-shell Cu-Ni nanoporous metal by molecular dynamics simulation [11]. The improvement of the mechanical properties seems partly linked to the presence of many interfaces, as in Cu-Nb composite nano-architected materials [5]. Core-shell (Al - amorphous-Si) nanostructures have also been shown to be resistant to cyclic indentation [12] due to core confinement [13]. Interestingly, restoration shape has also been reported experimentally in Ag - amorphous-SiO₂ NWs under bending [14].

The goal of the present study is to better un-

Email addresses:
maxime.guillotte@univ-poitiers.fr (Maxime Guillotte),
julien.godet@univ-poitiers.fr (Julien Godet),
laurent.pizzagalli@univ-poitiers.fr (Laurent Pizzagalli)

derstand the mechanical properties under cyclic loading of core-shell nanostructures combining high strength and good ductility. Core-shell NWs have been considered for their 1D shape, that allows an easier understanding of mechanical properties. Gold is used for the core for its good ductile property [15], while the shell is done with amorphous silicon taken as high strength material (at least at small dimensions [16, 17] and compared to gold).

In a previous work, we observed that such a hard amorphous shell is at the origin of plasticity confinement, resulting in an almost perfect elasto-plastic behaviour of core-shell NW, with shape conservation [18]. Here, we examined whether plasticity confinement could be retained during cyclic loading, by using molecular dynamics (MD) simulations. We first considered a bare gold NW at 300 K as a reference. Then, we performed similar calculations on gold-silicon core-shell NWs at 300 K and 1 K to unravel the effects of both the amorphous shell and the temperature. The results are discussed in the last section of this paper.

2. Methods

Our work is based on MD simulations, carried out with the open-source code LAMMPS [19]. We used a Modified Embedded Atom Method (MEAM) potential that has been previously optimized to describe Au-Si interactions [18]. The timestep used throughout the study is $\Delta t = 1$ fs to ensure time integration stability. In order to model the Au-Si core-shell NW (AuSi NW), we first build an amorphous silicon cylinder, before replacing its core by crystalline gold. The amorphous silicon NW is created by randomly placing silicon atoms in a cylinder of principal axis \hat{z} , with a length $L_z = 203.5$ Å, a radius of 120 Å and centered in $x = 0$ and $y = 0$. Periodic boundary conditions are used in \hat{z} direction. Using a conjugate gradient algorithm, we make a first rough energy minimization to move apart atoms which are initially too close from each other. A MD run is next performed at 2200 K in the NVT ensemble (constant number of atoms, volume and temperature) during 100 ps. The system is then quenched from 2200 K to 1 K during 250 ps and finally a conjugate gradient energy minimization is done. The radial distribution function of the amorphous silicon obtained by this method is consistent with previous studies [20, 21, 22] (Fig. 1).

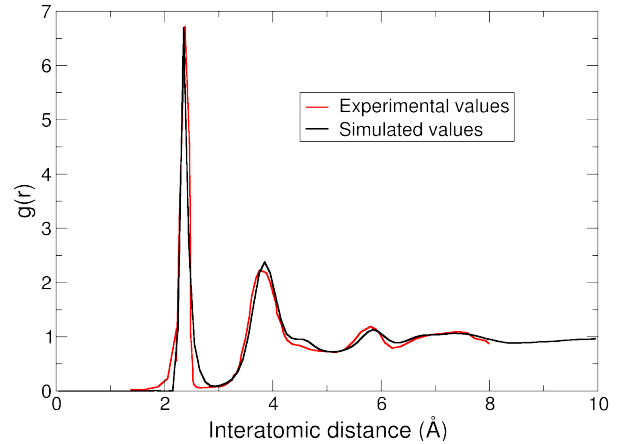


Figure 1: Radial distribution function of an experimental amorphous silicon [21] (red curve) ; Radial distribution function of our simulated amorphous silicon after the thermalization at 300 K (black curve).

In a second step, a cylinder of principal axis \hat{z} , centered in $x = 0$ and $y = 0$, with a radius of ≈ 61 Å and a length L_z along \hat{z} is defined. This volume is emptied and next filled with FCC gold atoms according to the following crystallographic orientations: $\hat{x} = [\bar{1}10]$, $\hat{y} = [001]$, $\hat{z} = [110]$. The gold lattice parameter for this potential is $a = 4.07$ Å. A MD run is then performed at 300 K during 1 ns and the dimension along \hat{z} is allowed to change in order to decrease the residual stress σ_{zz} along the \hat{z} axis to 0 GPa. This run was long enough to thermalize the system. The relaxed system is characterized by a length of 203.7 Å, a gold core radius R_{core} of ≈ 60 Å and a silicon shell thickness e of ≈ 45 Å, which corresponds to 137101 Au atoms and 222256 Si atoms. In addition, we prepare a pure gold NW (Au-NW) containing as many atoms as in the core of the AuSi-NW, with the same crystallographic orientations. After \hat{z} -relaxation at 300 K during 1 ns, final length and radius R_{Au} were 205 Å and ≈ 59 Å respectively. This run was long enough to thermalize the system. We performed NVT tension-compression deformation cycles on AuSi-NW at 300 K and 1 K as well as on Au-NW at 300 K, by tuning the box dimension along \hat{z} . The engineering strain rate is equal to 10^8 s $^{-1}$, which is typical of MD simulations. The maximum deformation reached in our simulations corresponds to an engineering strain of 30 %. To determine the engineering stress, the computed load is divided by the wires section before deformation $(\pi(R_{core} + e)^2$

and $\pi(R_{Au})^2$ for the AuSi-NW and the Au-NW, respectively).

3. Results

3.1. Au-NW at 300K

We first focus on the Au-NW, since its behavior during cyclic deformation will serve as a reference for the AuSi-NW study. Fig. 2 shows the engineering stress versus the engineering strain for four tension-compression cycles on Au-NW at 300 K. During the first tensile loading, the Au-NW is elastically deformed until $\epsilon = 5.0$ % with a Young modulus of 74 GPa. The first plastic event is an avalanche of spatially and temporally correlated dislocations [18] leading to the nucleation and growth of a twin as already shown in [23, 24], and the nucleation of a lonely dislocation leading to an isolated stacking fault. We carried out a dislocation analysis with the visualization and analysis software Ovito [25] for a range of deformations corresponding to the first drop of the black curve in Fig. 2. Three Shockley partial dislocations (propagating in the $[11\bar{2}]$ and $[\bar{1}12]$ directions in three consecutive (111) planes) are nucleated one after another leading to twin formation. A snapshot of the microstructure just after the first stress drop at $\epsilon = 5.2$ % is shown in Fig. 3(b). Up to $\epsilon = 14.6$ %, the plastic deformation mainly corresponds to the growing of this twin (Fig. 3 (b-c)), by the propagation of leading partial dislocations on the upper twin boundary plane and along $[11\bar{2}]$ (Fig. 3(b-c)). Between $\epsilon = 14.6$ % and $\epsilon = 30$ %, the plastic deformation is next associated with full slip (propagation of dissociated perfect dislocations) on the upper twin boundary plane (Fig. 3(c-d)).

Experimentally, in thin films, the transition from twinning to full dislocation slips has been attributed to the increase of the films thickness [26]. In NWs, however, twin formation is not necessarily followed by dislocations slip, but rather by twinning on conjugate slip planes [27]. In our calculations, we observed a transition from twinning to full slip, in agreement with previous atomistic simulations [23, 28]. This difference between experiments and simulations might be partly explained by the crystal re-orientation caused by twinning and the use of periodic boundary conditions in simulations, whereas experimentally NW ends are clamped. In the simulation, as the twin size increases, the stress axis slightly tilts, thus modifying the Schmid factors on leading (from 0.471 to 0.498) and on trailing

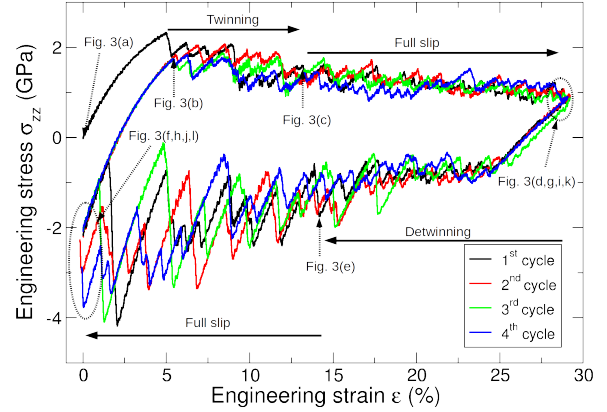


Figure 2: Engineering stress - engineering strain curves for 4 tension-compression cycles done at 300 K for Au-NW.

partial dislocations (from 0.236 to 0.242) before and after the twin formation. In addition, the growth of a single twin leads to ledges formation at the intersection of surface and twin boundaries, which act as local stress concentrators for dislocations nucleation [29]. These two effects enhance the nucleation probability of leading, but also trailing partial dislocations. Once a trailing dislocation is nucleated, a sharp step is created on the surface, which increases the stress concentration on a unique slip plane leading to the emission of several dissociated perfect dislocations in a single plane. This mechanism of twinning followed by full slip during tensile loading, greatly affects the morphology of the Au-NW, as shown in Fig. 3(d).

During unloading, the Au-NW is elastically deformed between $\epsilon = 30$ % and $\epsilon = 24.4$ %. From 24.4 % to 14.2 %, detwinning occurs by the nucleation and migration of partial dislocations in the lower twin boundary plane (Fig. 3(d)). After detwinning, the plastic deformation is associated to multiple dislocations slip in the same plane between $\epsilon = 14.2$ % and $\epsilon = 0$ % (Fig. 3(e-f)). The sequence of twinning followed by full slip in traction, and detwinning followed by full slip in compression, is related to different Schmid factors on the leading and trailing partial dislocations for traction and compression, as explained in previous works [30, 31, 32]. Note that twinning and dislocation slips can also depend on the surface roughness of NWs as already shown in Ref. [30].

In compression, serrated stress variations have a larger amplitude than in tension, due to the cas-

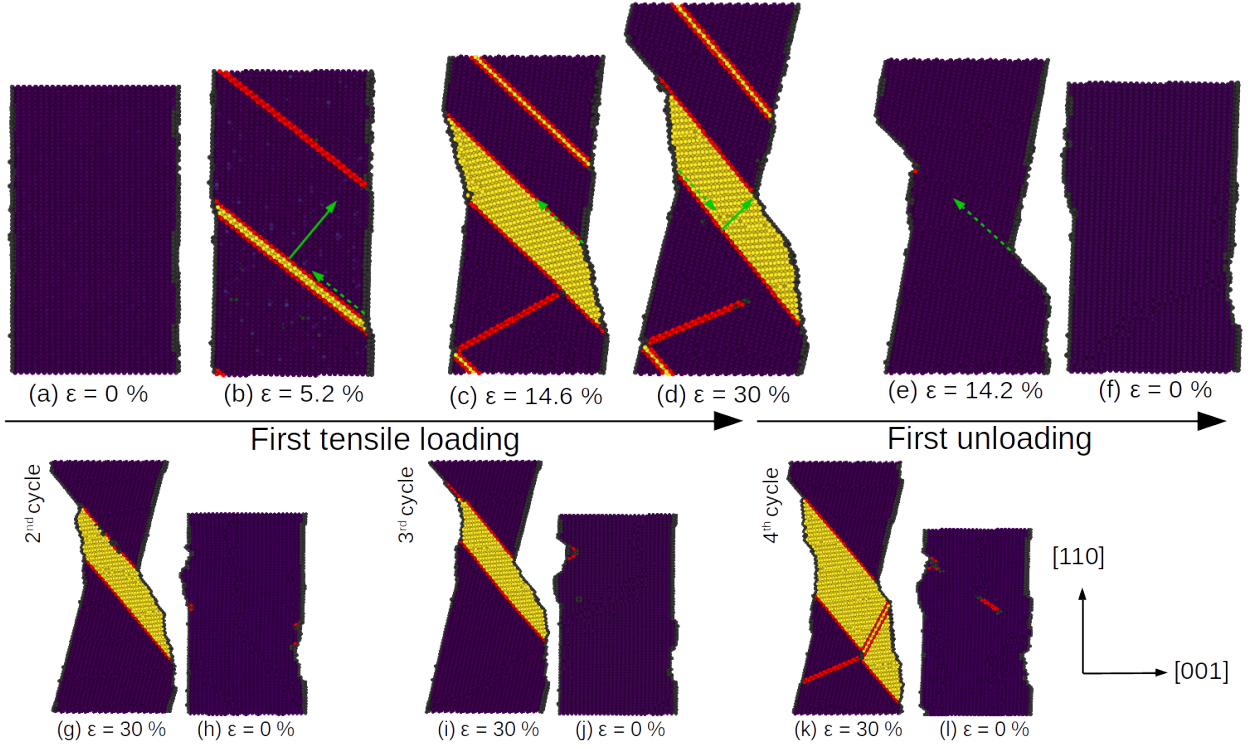


Figure 3: Evolution of Au-NW structure (cross-section views) during the first cycle (a-f). Structures at the end of the second, third and fourth tensile loading (g,i,k respectively) and structures at the end of the second, third and fourth compressive loading (h,j,l respectively). Purple, yellow, red and grey spheres show respectively Au atoms of the parent crystal (FCC environment), Au atoms of the twinned crystal (FCC environment), Au atoms in HCP environment and Au atoms in unknown environment. The full (dashed) line arrows indicate the direction of twin boundaries (dislocation) motion.

cading nucleation of full dislocations. Conversely, under tensile loading, dislocations tend to be emitted one by one (Fig. 2). Moreover, full dislocations migrate in the same slip plane, and each nucleation event increases the surface step height under tensile loading (Fig. 3(e-f)). Since stress concentration increases with step height, lower applied stress are required for nucleating additional dislocations. Instead, in compression, each nucleated dislocation decreases the step height (Fig. 3(e-f)), and nucleating further dislocations requires larger applied stresses.

After full unloading, the wire globally recovers its shape and all the crystallographic defaults in the bulk (stacking faults and twins) are healed (Fig. 3(f)). However, the NW surface is now rougher and the wire at $\epsilon = 0 \%$ is in a compressive state ($\sigma_{zz} \approx -2$ GPa). This can be explained by the fact that there were less dislocation slip events during unloading than loading stage, and thus the NW stretching is not fully compensated over the four

cycles.

During the second cycle, the Au-NW is elastically deformed from $\epsilon = 0 \%$ to $\epsilon = 5.3 \%$ and the new mechanical equilibrium ($\sigma_{zz} = 0$) is reached at $\epsilon = 2.4 \%$. For the rest of this cycle and during the subsequent cycles, twinning is followed by full dislocation slips during tensile loading, while during compressive loading, detwinning is followed by dislocation slips. For second and subsequent cycles, yield points are quasi equivalent and the stress-strain curves are almost superimposed. Note that the yield stresses are slightly lower than the value obtained for the first cycle, essentially because surface defects created during the first cycle facilitate the plastic deformation for the next cycles compared to the initial pristine system. We also observed that the surface roughness increases with cycles, at $\epsilon = 0 \%$ (Fig. 3(f,h,j,l)) and at $\epsilon = 30 \%$ (Fig. 3(d,g,i,k)).

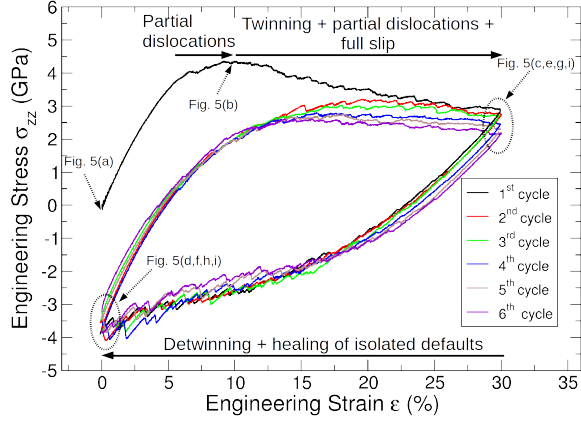


Figure 4: AuSi-NW engineering stress - engineering strain curves for 6 tension-compression cycles done at 300 K.

3.2. AuSi-NW at 300K

Fig. 4 shows engineering stress versus engineering strain curves for six tension-compression cycles and the core-shell AuSi-NW, at 300 K. During the first tensile loading, the AuSi-NW is elastically deformed until $\epsilon = 5.8$ %, with a Young modulus equal to 90 GPa, larger than the Au-NW one because of the silicon shell. The stress-strain curves do not show the sawtooth behavior (Fig. 4) as obtained for Au-NW (Fig. 2). Indeed, from 5.8 % to 10.1 %, only partial dislocations are nucleated, with no dislocations avalanche, thus limiting stress drops. Also, there is no spatial correlation between two successive dislocations, as well as no twin formation (Fig. 5(b)). The silicon shell is the main factor limiting dislocation cascades, and delaying twin growth. At strains greater than $\epsilon = 10.1$ %, twins begin to grow, accompanied by the nucleation and propagation of isolated full and partial dislocations (Fig. 5(b-c)). Due to the silicon shell confinement, dislocations are homogeneously distributed all along the interface and the NW core morphology is preserved. However, roughness of the shell surface increases compared to the initial structure. During the first unloading, the AuSi-NW is elastically deformed between $\epsilon = 30$ % and $\epsilon = 25$ %. From $\epsilon = 25$ % to $\epsilon = 0$ %, similar plastic deformation mechanisms than during loading are observed, i.e. nucleation of partial dislocations in adjacent planes leading to detwinning, and nucleation and propagation of isolated partial and full dislocations (Fig. 5(c-d)). At the end of the first unloading, all bulk defects in the core have been healed. However, both the shell surface and the core-shell inter-

face appear slightly rougher compared to the initial state. Furthermore, a limited interdiffusion is occurring at the interface, in agreement with a previous work on Au-Ni core-shell NW [33]. Note that the AuSi-NW is in a compressive state at $\epsilon = 0$ % ($\sigma_{zz} \approx -3.7$ GPa), like Au-NW after the first cycle, for similar reasons.

During the second cycle, the NW is elastically deformed until $\epsilon = 6.7$ % and reach mechanical equilibrium at $\epsilon = 4.9$ % (Fig. 4). The stress-strain curve is different from that of the first cycle, with a lower stress maximum occurring at a larger strain. The flow stress is also slightly lower although plasticity mechanisms are similar. However, the unloading part closely resembles the one in the first cycle, both in terms of stress variations and deformation mechanisms. Stress-strain curves are almost superimposed for the following cycles, except regarding the stress reached at maximum strain. In fact, the latter clearly decreases as the numbers of cycles grow. Examining in details the morphology of the AuSi NW during cycles, one can observe the formation of trenches at the shell surface (Fig. 5(c,e,g,i)), deepening as a function of cycles. Those are only partially healed during the unloading stages (Fig. 5(d,f,h,j)). Furthermore, cyclic deformation tends to slowly change the core morphology, in an apparent relation with shell trenches.

We also tested the influence of the shell thickness on the mechanical properties of the AuSi-NW. We found that the stress-strain curve and the deformation mechanisms obtained with a shell as thin as 1 nm, are similar to those obtained with the larger shell of 4.5 nm (See Supplementary Material). This suggests that the results presented in this work are not specific to systems with thick shells.

3.3. AuSi-NW at 1K

In order to study the influence of the temperature, four tension-compression cycles have been performed for the AuSi-NW, at 1 K. The calculated stress-strain curves are shown in Fig. 6. Compared to the 300 K test, the elastic deformation stage lasts until $\epsilon = 5.8$ %, with a Young modulus of 110 GPa. This is higher than at 300 K, in agreement with the well accepted fact that the materials stiffness is greater at 0 K than at 300 K. For the four tensile loadings, identified plastic events include a few isolated partial dislocations and a few isolated dissociated perfect dislocations, and mainly the growth of a unique twin (Fig. 7(a,c,e,g)). At the highest strains, this large twin induces a necking of the gold

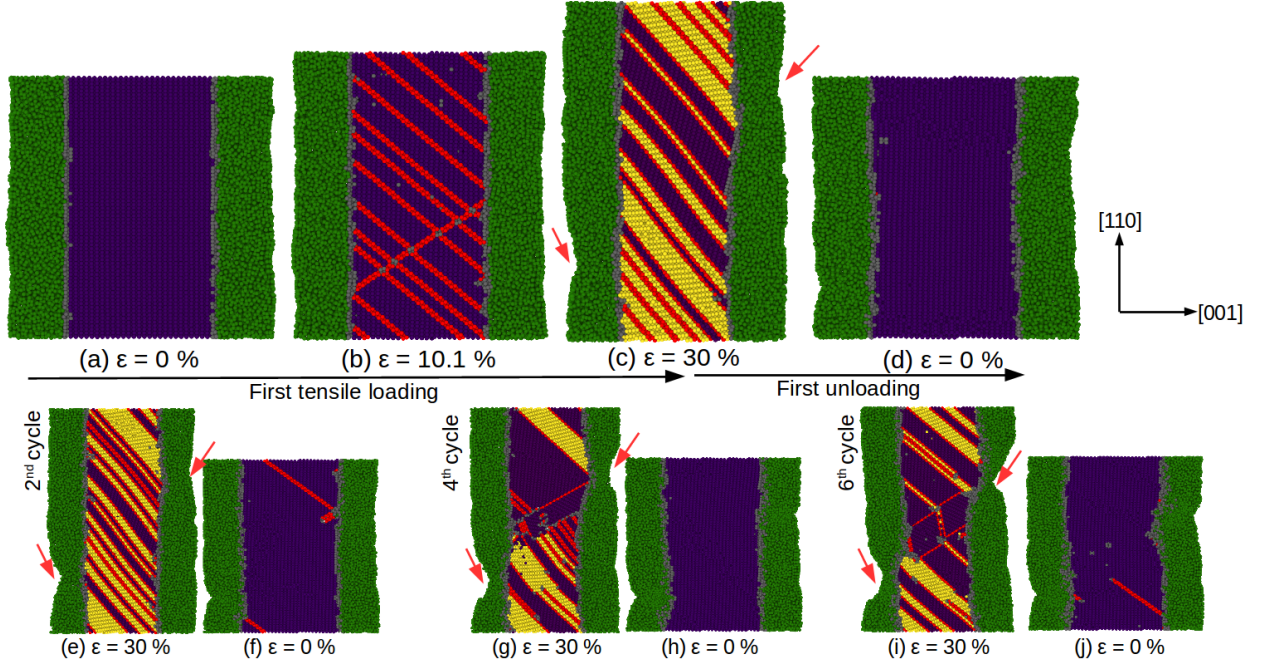


Figure 5: Evolution of AuSi-NW structure (cross-section views) during the first cycle (a-d). Structures at the end of the second, fourth and sixth tensile loading (e,g,i respectively) and structures at the end of the second, fourth and sixth compressive loading (f,h,j respectively). Purple, yellow, red, grey and green spheres are respectively Au atoms of the parent crystal (FCC environment), Au atoms of the twinned crystal (FCC environment), Au atoms of HCP environment, Au atoms of unknown environment and silicon atoms. The red arrows indicate the location of trenches which form on shell surface during cycles.

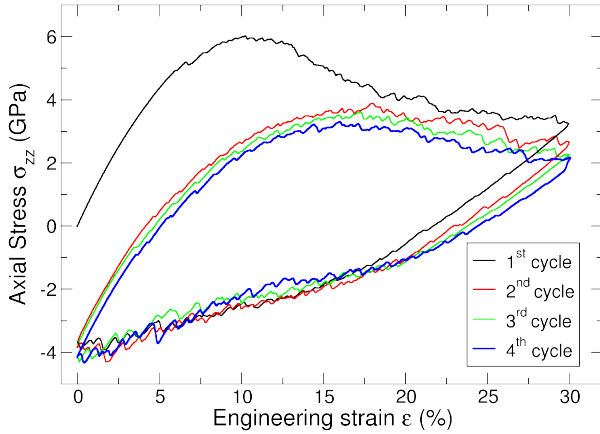


Figure 6: AuSi-NW engineering stress - engineering strain curves of 4 cycles tension-compression performed at 1 K.

core, correlated to the formation of deep and large trenches in the silicon shell. However, the core necking is lighter than the one occurring at the upper twin boundary in the bare Au-NW.

During unloading stages, the activation of plastic deformation mechanisms like detwinning allows for

recovering a gold core containing no or few residual defects (Fig. 7(b,d,f,h)). The opened trenches in the shell are also partially bridged. However, both the shell and the core morphology keep stigma associated to the cyclic deformation.

4. Discussion

4.1. The singularity of the first loading

For all tested systems, we find that the stress variations monitored during the first loading are different than those obtained for the following cycles. In particular, larger maximum stress values are reached (See Fig. 2, 4, and 6). This is especially true for core-shell systems. We tentatively attribute this result to structural changes between the initial state and the beginning of the second loading. For instance, the starting configuration for the pure gold NW is alike a perfect cylinder without any surfaces defects. After the first cycle, the surface is more rough, with the presence of atomic steps left by dislocations. It is well known that such surface defects are efficient stress concentrators [29], favoring the nucleation of dislocations at

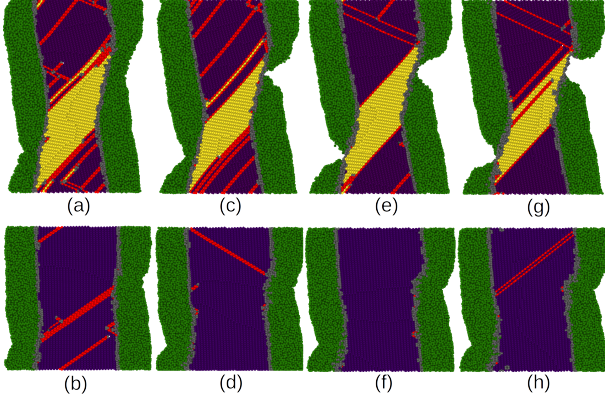


Figure 7: At 1 K: Microstructures at the end of the first, second, third and fourth tensile loading (a,c,e and g respectively) and microstructures at the end of the first, second, third and fourth compressive loading (b,d,f and h respectively) (See Fig. 5 for color coding).

a lower applied stress. For the core-shell NW, a low density of defects is present at the Au-Si interface for the initial structure, due to long annealing and relaxation. After the first cycle, the amount of interface defects has substantially increased, as well as the interface roughness (Compare Fig. 5-a and Fig. 5-d). Again, it facilitates the nucleation of the first dislocations, which then happened at a lower applied stress than during the first cycle.

The singularity of the first loading compared to the followings ones is then related to the use of initial configurations with no or few structural defects. It is also probably an indirect consequence of the high strain rates used in molecular dynamics simulations. In fact, the short simulation time does not allow for an efficient thermal annealing of the structural defects left by plastic deformation. The influence of thermal annealing can be easily estimated by comparing the stress - strain curves and configurations at 300 K (Figs. 4-5) and 1 K (Figs. 6-7), respectively. At 300 K, the maximum stress drops by about 1.1 GPa between the first and second cycle, whereas it is about 2.1 GPa at 1 K. The interface roughness is also more pronounced at 1 K than at 300 K. These observations suggest that in experiments, with characteristic times of the order of the minute or the hour, the difference between the first cycle and the following ones should be greatly reduced compared to the present work.

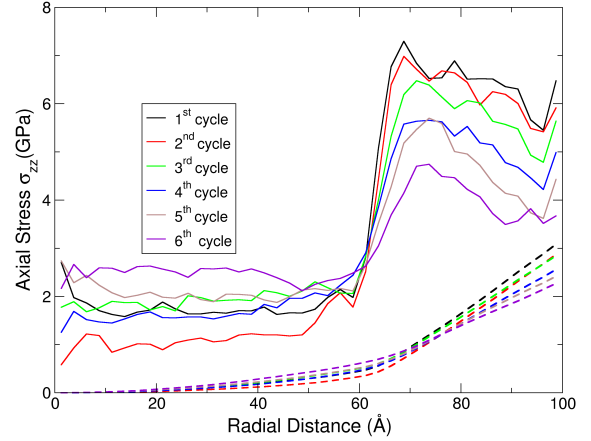


Figure 8: Average axial stress of the AuSi-NW at $\epsilon = 30\%$ during the cyclic deformation at 300 K as a function of the radial distance for each cycle (full lines). Stress integrated on a cylinder of radius r and divided by the area of the initial cross section S_0 ($\int_0^r 2\pi r \sigma dr / S_0$) (dashed lines).

4.2. Reversibility of the Au NW plastic deformation

Putting aside the first cycle and focusing only on the following ones, the stress - strain curves for the Au NW seem to indicate that the plastic deformation is reversible (Fig. 2). This feature is related to the fact that twinning is the favored mode of deformation at low strains. This mechanism is at the origin of the well documented pseudoelastic behavior of metallic nanowires with square and rhombic cross sections [23, 27, 34]. However, in the present work, twinning is always accompanied with full dislocation slip events, probably because of the size and circular cross-section of the NW. Dislocation slip leads to a significant shearing of the NW which is only partially healed during unloading, conversely to twinning. This is confirmed by the seemingly roughness increase of the Au NW surface during cycles (Fig. 4). The cyclic deformation of the Au NW is then better described as quasi-reversible. Note that only a limited number of cycles have been performed in this work, and it is not clear whether additional cycles will continue to change the NW structure, or if a stable state will be reached.

4.3. Reversibility of the AuSi NW plastic deformation

We now discuss the reversibility of the AuSi NW plastic deformation under cyclic deformation. At both 300 K (Fig. 4) and 1 K (Fig. 6), the stress -

strain curves show a significant overlap for the second and next cycles. However the reversible character is less prominent than for bare Au NW, in particular the stress values at high strain now decrease as a function of cycles. For further insights, we plot in Fig. 8 the axial stress from the NW center to its surface, at $\epsilon = 30\%$, 300 K and for each cycle. The curves are obtained by computing the mean atomic stress concentric hollow cylinders with equal thickness at different radii. When integrated over the whole NW (dashed curves in Fig. 8), the stress values at 30 % as reported in Fig. 4 are recovered.

Examining first the core part (for distance lower than 60 Å), there is no clear trend regarding the stress variations between each cycle. Those latter are due to different core structures after each loading. Conversely, in the shell part, the axial stress decreases as a function of cycles. It is noteworthy that the more the radial distance increases, the more the weight of the stress contribution to the mean stress is important, since the number of atoms contained in a cylinder is proportional to its squared radius. This is evidenced by integrating the axial stress on a cylinder of increasing radius (Fig. 8, dashed curves). Therefore, the stress decrease as a function of cycles observed in Figs. 4, 6 can be mainly attributed to the shell.

The analysis of the evolution of the amorphous shell structure over cycles reveals the progressive formation of trenches on the shell surface, that weakens the shell mechanical resistance to loading, and is certainly the cause of the aforementioned stress decrease. The consequences are more dramatic at 1 K, with a localized breaking of the shell (Fig. 7-a,c,e,g and 9-a,b). These figures show a spatial correlation between the large twin formed in the core and those trenches, at $\epsilon = 30\%$. During tensile loading, the formation of the twin leads to crystal rotation and core necking, generating shear strain in the shell. In fact, examining the atomic shear strain just before the rupture of the shell suggests that the largest values correspond to twin regions in the vicinity of the trenches (Fig. 9-c). The combination of this shear strain with the applied tensile stress induces a mixed loading on the shell under mode 1 and 2 leading to the expansion of the trenches, and potentially to shell fracture. This analysis is in agreement with the brittle nature of silicon, in particular at low temperature [35, 36].

All these elements indicate that the deformation of AuSi-NW under cyclic loading is not perfectly

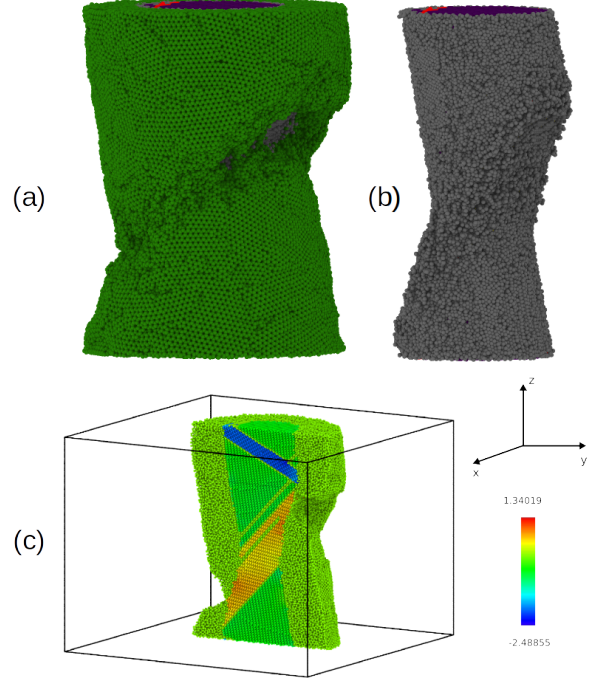


Figure 9: (a-b) 3D representations of the AuSi-NW at the end of the fourth tensile loading at 1 K, (a: full Au-Si-NW, b: gold core only). A cross-sectional view is shown in Fig. 7(g). The color coding is the same than in Fig. 3, 5 and 7. (c) Atomic shear strain associated to core gold atoms in AuSi-NW for the same system.

reversible, and that the irreversible part can be essentially ascribed to the shell. We propose the following scenario. During loading, there is a stress build-up on silicon atoms which is only partially relaxed by small atomic displacements, typical of amorphous plastic deformation. At high strains, a more efficient stress relaxation is obtained by the breaking of silicon bonds, leading to the formation of trenches. The shell structure integrity is not fully recovered during unloading (Fig. 7-d,f,h), resulting in the progressive opening of the trenches.

4.4. Influence of various parameters on shell weakening

In this part we examine the effect of different parameters on the weakening of the Si shell, and thus on the reversibility of the AuSi plastic deformation. Two different temperatures, 300 K and 1 K, have been tested in this work. Comparing stress - strain curves, in Figs. 4 and 6, indicates that the reversible character is stronger at 300 K than at 1 K. In fact, the stress at 30% decrease by 0.5 GPa from the first to the fourth cycle in

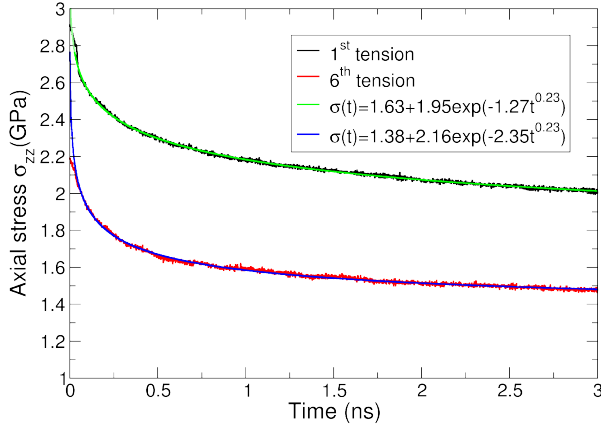


Figure 10: Evolution of the AuSi NW engineering stress during thermal annealing, for two initial configurations corresponding to NW pulled at 30%, at the end of the first and the sixth tensile loading (black and red curves respectively), with their fitting curves (green and blue curves respectively).

the former case, whereas the stress reduction is about 1.1 GPa in the latter case. This suggests a thermally activated recovery of the Si shell during the consecutive extension-compression cycles. This conclusion is supported by the examination of the shell structure and morphology. Significant cracks already occurs during the 2nd cycle at 1 K (Fig. 7), although at 300 K the shell is not fully broken even after the 6th cycle (Fig. 5). Overall, the morphology of the shell is more preserved at 300 K than at 1 K.

Another important factor is the strain rate inherently used in MD simulations, which is typically 10^{11} times higher than in experiments. Such a large difference makes it almost impossible to use the same procedure to study the effect. In fact, decreasing the strain rate to 10^7 s⁻¹ or even lower would require a large increase of computational resources, with a likely unnoticeable influence. To circumvent this issue, we carried out additional NVT calculations at fixed strain (30%), which then mimic a deformation test with an infinitely slow strain rate. The Fig. 10 shows the results obtained at 300 K over a MD time of 3 ns, for two structures obtained by cyclic deformation at a strain of 30% and at cycles one and six. For the first (sixth) cycle, the axial stress decreases from 2.9 GPa to 2 GPa (from 2.2 GPa to 1.5 GPa). This result suggests that significantly reduced stresses would be obtained if low strain rates could be used in MD simulations. At 10^8 s⁻¹, there is not enough time for thermally acti-

vated stress relaxation mechanisms to occur, which leads to stress build-up in localized regions, and finally trenches formation and cracks propagation. The stress variations in Fig. 10 have been fitted with exponentially decreasing functions (fitting parameters reported in the figure), to estimate the residual axial stress at times greater than 3 ns. Choosing 1 s as a time typical for experimental deformation of nanowires, the axial stress is extrapolated to 1.63 GPa for the first, and 1.38 GPa for the sixth cycle. The difference between these two values is only 0.25 GPa, to be compared to the initial stress difference of 0.75 GPa between the first and the sixth cycles (at 30% in Fig. 4). Therefore, the extrapolation to times comparable to experiments suggests a significant improvement of the amorphous shell and by consequence of the reversibility of the plastic deformation of the core-shell nanowire during cyclic deformation.

At last, the influence of the maximum strain attained during tensile loading is discussed. Cyclic deformation of the AuSi NW between 0% and 9% have been carried out at 1 K, for three cycles. This specific strain value has been selected since it corresponds to the strain threshold above which twinning is occurring. The stress - strain curves and snapshots of 9% strained configurations are shown in Supplementary Materials. They reveal a greatly improved reversibility compared to the case with 30% maximum strain. In fact, there is now no stress decrease at maximum strain after the first cycle. Also the shell appears to be completely preserved during the cyclic deformation. Consequently, it can continue to confine and spatially delocalize the plastic deformation in the gold core with maximal efficiency.

5. Conclusion

In this work, we focused on the mechanical properties of gold NWs and Au-Si core-shell NWs during cyclic loading, in order to investigate the influence of a hard amorphous silicon shell on gold NW. We first observed an increase of the yield stress due to the presence of the hard shell, compared to pure gold NW. We also found that a hard shell can confine the plasticity in the core, leading to shape conservation at deformation as large as 30% in tension over several cycles. The presence of the shell favors twins, isolated partials and isolated full dislocations over localized full dislocations. This allows for a seemingly macroscopic reversible plas-

ticity, with the presence of interface defects. Usually, the mechanisms of reversible plasticity is based on twinning and detwinning that allows for an homogeneous distribution of plasticity all along the NW length. Here, the hard amorphous shell favors not only twinning but also an homogeneous distribution of full dislocations. Therefore, a larger amount of plastic strain could be stored in these composite core-shell NWs than in Au NWs, which should lead to reversible plasticity at larger strain. However, we also found that the reversible plasticity effect is progressively lost at 300 K over cycles and completely lost at 1 K after the first loading. The analysis of thermal annealing of strained core-shell NW at 300 K on a long timescale, suggest that the high strain rate in MD simulations induces a limited self-healing of the amorphous shell, thus leading to defects storage during cyclic loading. These defects appear as precursors of cracks and shell rupture. Additional analyses also show that shell degradation can be greatly reduced if the maximum loading strain remains below the threshold above which twinning is occurring. Our investigations imply that optimizing these different factors (temperature, strain rate, maximum loading strain) could enhance the reversibility of the plastic deformation during cyclic tests. This obviously suggests potential directions for future researches.

Acknowledgements

This work pertains to the French Government program Investissements d'Avenir (LABEX INTERACTIFS, reference ANR-11-LABX-0017-01). Computations have been performed on the supercomputer facilities of the Mésocentre de calcul Poitou-Charentes.

References

- [1] Hongti Zhang, Jerry Tersoff, Shang Xu, Huixin Chen, Qiaobao Zhang, Kaili Zhang, Yong Yang, Chun-Sing Lee, King-Ning Tu, Ju Li, and Yang Lu. Approaching the ideal elastic strain limit in silicon nanowires. *Science Advances*, 2(8), 2016.
- [2] M. D. Uchic, D. M. Dimiduk, J. N. Florando, and W. D. Nix. Sample dimensions influence strength and crystal plasticity. *Science*, 305:986, 2004.
- [3] A. Misra, J.P. Hirth, and R.G. Hoagland. Length-scale-dependent deformation mechanisms in incoherent metallic multilayered composites. *Acta Materialia*, 53(18):4817 – 4824, 2005.
- [4] T. Zhu and J. Li. Ultra-strength materials. *Prog. Mater. Sci.*, 55:710–757, 2010.
- [5] T. Gu, O. Castelnau, S. Forest, E. Hervé-Luanco, F. Lecouturier, H. Proudhon, and L. Thilly. Multiscale modeling of the elastic behavior of architected and nanostructured cu-nb composite wires. *International Journal of Solids and Structures*, 121:148 – 162, 2017.
- [6] Y. S. Zhang, Y. H. Zhao, W. Zhang, J.W. Lu, J. J. Hu, W. T. Huo, and P. X. Zhang. Core-shell structured titanium-nitrogen alloys with high strength, high thermal stability and good plasticity. *Scientific Reports*, 7:40039, 2017.
- [7] Yujie Chen, Qiang Gao, Yanbo Wang, Xianghai An, Xiaozhou Liao, Yiu-Wing Mai, H. Hoe Tan, Jin Zou, Simon P. Ringer, and Chennupati Jagadish. Determination of young's modulus of ultrathin nanomaterials. *Nano Letters*, 15(8):5279–5283, 2015.
- [8] Bin Zheng, Yi Nong Wang, Min Qi, and Elissa H. Williams. Phase boundary effects on the mechanical deformation of core/shell cu/ag nanoparticles. *Journal of Materials Research*, 24(7):2210–2214, 2009.
- [9] D. Kilymis, C. Gérard, and L. Pizzagalli. Ductile deformation of core-shell si-sic nanoparticles controlled by shell thickness. *Acta Mater.*, 164:560–567, feb 2019.
- [10] Monika M. Biener, Juergen Biener, Andre Wichmann, Arne Wittstock, Theodore F. Baumann, Marcus Baeumer, and Alex V. Hamza. ALD Functionalized Nanoporous Gold: Thermal Stability, Mechanical Properties, and Catalytic Activity. *Nano Letters*, 11(8):3085–3090, 2011.
- [11] Lijie He and Niaz Abdollahim. Deformation mechanisms and ductility enhancement in core-shell cu@ni nanoporous metals. *Computational Materials Science*, 150:397 – 404, 2018.
- [12] Jason G. Steck, Robert A. Fleming, Josue A. Goss, and Min Zou. Deformation and fatigue resistance of al/a-si core-shell nanostructures subjected to cyclic nanoindentation. *Applied Surface Science*, 433:617 – 626, 2018.
- [13] Robert A. Fleming and Min Zou. The effects of confined core volume on the mechanical behavior of al/a-si core-shell nanostructures. *Acta Materialia*, 128:149 – 159, 2017.
- [14] Sergei Vlassov, Boris Polyakov, Leonid M. Dorogin, Mikk Vahtrus, Magnus Mets, Mikk Antsov, Rando Saar, Alexey E. Romanov, Ants Lhmus, and Rnno Lhmus. Shape restoration effect in agsio2 coreshell nanowires. *Nano Letters*, 14(9):5201–5205, 2014.
- [15] Seunghwa Ryu, Christopher R. Weinberger, Michael I. Baskes, and Wei Cai. Improved modified embedded-atom method potentials for gold and silicon. *Modelling Simul. Mater. Sci. Eng.*, 17(7), 2009.
- [16] K. Kang and W. Cai. Brittle and ductile fracture of semiconductor nanowires - molecular dynamics simulations. *Phil. Mag.*, 87(14-15):2169, 2007.
- [17] Fredrik Östlund, Karolina Rzepiejewska-Malyska, Klaus Leifer, Lucas M. Hale, Yuye Tang, Roberto Ballarini, William W. Gerberich, and Johann Michler. Brittle-to-Ductile Transition in Uniaxial Compression of Silicon Pillars at Room Temperature. *Adv. Funct. Mater.*, 19(15):2439–2444, 2009.
- [18] Julien Godet, Clarisse Furgeaud, Laurent Pizzagalli, and Michael J. Demkowicz. Uniform tensile elongation in au-si core-shell nanowires. *Extreme Mechanics Letters*, 8:151–159, 2016.
- [19] S. Plimpton. Fast parallel algorithms for short-range molecular dynamics. *J. Comp. Phys.*, 117:1–19, 1995.
- [20] Arthur France-Lanord, Etienne Blandre, Tristan Al-

- baret, Samy Merabia, David Lacroix, and Konstantinos Termentzidis. Atomistic amorphous/crystalline interface modelling for superlattices and core/shell nanowires. *Journal of Physics: Condensed Matter*, 26(5):055011, 2014.
- [21] Khalid Laaziri, S. Kycia, S. Roorda, M. Chicoine, J. L. Robertson, J. Wang, and S. C. Moss. High resolution radial distribution function of pure amorphous silicon. *Phys. Rev. Lett.*, 82:3460–3463, 1999.
- [22] Andreas Pedersen, Laurent Pizzagalli, and Hannes Jns-son. Optimal atomic structure of amorphous silicon obtained from density functional theory calculations. *New J. Phys.*, 19(6):063018, 2017.
- [23] Wuwei Liang and Min Zhou. Atomistic simulations reveal shape memory of fcc metal nanowires. *Physical Review B*, 73(11), 2006.
- [24] Qing-Jie Li, Ju Li, Zhi-Wei Shan, and Evan Ma. Surface rebound of relativistic dislocations directly and efficiently initiates deformation twinning. *Phys. Rev. Lett.*, 117:165501, Oct 2016.
- [25] Alexander Stukowski. Visualization and analysis of atomistic simulation data with ovito - the open visualization tool. *Modelling Simul. Mater. Sci. Eng.*, 18(1):015012, 2010.
- [26] S.H. Oh, M. Legros, D. Kiener, P. Gruber, and G. Dehm. In situ tem straining of single crystal au films on polyimide: Change of deformation mechanisms at the nanoscale. *Acta Mater.*, 55(16):5558 – 5571, 2007.
- [27] Subin Lee, Jiseong Im, Youngdong Yoo, Erik Bitzek, Daniel Kiener, Gunther Richter, Bongsoo Kim, and Sang Ho Oh. Reversible cyclic deformation mechanism of gold nanowires by twinning-detwinning transition evidenced from in situ TEM. *Nature Communications*, 5, 2014.
- [28] Reza Rezaei and Chuang Deng. Pseudoelasticity and shape memory effects in cylindrical FCC metal nanowires. *Acta Materialia*, 132:49–56, 2017.
- [29] S. Brochard, P. Hirel, L. Pizzagalli, and J. Godet. Elastic limit for surface step dislocation nucleation in face-centered cubic metals: Temperature and step height dependence. *Acta Mater.*, 58(12):4182 – 4190, 2010.
- [30] Harold S. Park, Ken Gall, and Jonathan A. Zimmerman. Deformation of fcc nanowires by twinning and slip. *J. Mech. Phys. Solids*, 54(9):1862 – 1881, 2006.
- [31] Jong-Hyun Seo, Youngdong Yoo, Na-Young Park, Sang-Won Yoon, Hyoban Lee, Sol Han, Seok-Woo Lee, Tae-Yeon Seong, Seung-Cheol Lee, Kon-Bae Lee, Pil-Ryung Cha, Harold S. Park, Bongsoo Kim, and Jae-Pyoung Ahn. Superplastic deformation of defect-free au nanowires via coherent twin propagation. *Nano Letters*, 11(8):3499–3502, 2011.
- [32] Christopher R. Weinberger, Andrew T. Jennings, Keonwook Kang, and Julia R. Greer. Atomistic simulations and continuum modeling of dislocation nucleation and strength in gold nanowires. *Journal of the Mechanics and Physics of Solids*, 60(1):84–103, 2012.
- [33] Niaz Abdolrahim, David F. Bahr, Benjamin Revard, Cassandra Reilly, Jia Ye, T. John Balk, and Hussein M. Zbib. The mechanical response of core-shell structures for nanoporous metallic materials. *Philosophical Magazine*, 93(7):736–748, 2013.
- [34] Harold S. Park, Ken Gall, and Jonathan A. Zimmerman. Shape memory and pseudoelasticity in metal nanowires. *Phys. Rev. Lett.*, 95(25):255504, 2005.
- [35] S. Korte, J.S. Barnard, R.J. Stearn, and W.J. Clegg. Deformation of silicon - insights from microcompression testing at 25 - 500 degree c. *International Journal of Plasticity*, 27(11):1853 – 1866, 2011.
- [36] J. Rabier, P. O. Renault, D. Eyidi, J. L. Dermenet, J. Chen, H. Couvy, and L. Wang. Plastic deformation of silicon between 20c and 425c. *physica status solidi (c)*, 4(8):3110–3114, 2007.